# Enhanced simulations on the Athena/Wide Field Imager instrumental background

**Tanja Eraerds,[a,*] Valeria Antonelli,[a] Chris Davis,[b] David Hall,[b] Oliver Hetherington,[b] Andrew Holland,[b] Michael Hubbard,[b] Norbert Meidinger,[a] Eric Miller,[c] Silvano Molendi,[d] Emanuele Perinati,[e] Daniel Pietschner,[a] and Arne Rau[a]**

[a]Max-Planck-Institut für extraterrestrische Physik, Garching, Germany
[b]Open University, Centre for Electronic Imaging, Milton Keynes, United Kingdom
[c]MIT Kavli Institute for Astrophysics and Space Research, Cambridge, Massachusetts, United States
[d]IASF-Milano/INAF, Milan, Italy
[e]Universität Tübingen, Institut für Astronomie und Astrophysik, Tübingen, Germany

**Abstract.** The Wide Field Imager (WFI) is one of two focal plane instruments of the Advanced Telescope for High-Energy Astrophysics (Athena), ESA's next large x-ray observatory, planned for launch in the early 2030s. The current baseline halo orbit is around L2, and the second Lagrangian point of the Sun-Earth system L1 is under consideration. For both potential halo orbits, the radiation environment, solar and cosmic protons, electrons, and He-ions will affect the performance of the instruments. A further critical contribution to the instrument background arises from the unfocused cosmic hard x-ray background. It is important to understand and estimate the expected instrumental background and to investigate measures, such as design modifications or analysis methods, which could improve the expected background level to achieve the challenging scientific requirement ($<5 \times 10^{-3}$ counts/cm$^2$/keV/s at 2 to 7 keV). Previous WFI background simulations done in Geant4 have been improved by taking into account new information about the proton flux at L2. In addition, the simulation model of the WFI instrument and its surroundings employed in Geant4 simulations has been refined to follow the technological development of the WFI camera.  [DOI: 10.1117/1.JATIS.7.3.034001]

**Keywords:** Athena/WFI; instrumental background; space environment; particle environment; Geant4.

Paper 21010AS received Jan. 25, 2021; accepted for publication Jul. 15, 2021; published online Jul. 27, 2021.

## 1 Introduction

### 1.1 *Description of Wide Field Imager Instrument*

A comprehensive description of the Wide Field Imager (WFI) instrument is provided in Ref. 1. Here, we give a short summary of the main relevant components. This work is an update of Ref. 2 and hence contains similar descriptions of the WFI, key science drivers, background components, and the Monte Carlo simulation tool Geant4/GRAS.[3,4] The WFI will provide important scientific capabilities to the mission. The large detector array (LDA) will offer an unprecedented survey capability with its $40' \times 40'$ field of view (FOV) properly sampling the point spread function (5″ HEW on-axis) provided by the Athena mirror system.

This FOV is achieved by employing a large area, almost $14 \times 14$ cm$^2$-sized, silicon-based detector in the focal plane.

The signal electrons, generated by an incoming x-ray photon, are collected and amplified by active pixels sensors of depleted p-channel field-effect transistors (DEPFET) type, which are

*Address all correspondence to Tanja Eraerds, tanja.eraerds@mpe.mpg.de

integrated onto a backilluminated fully depleted 450-$\mu$m-thick silicon bulk. These are providing the state-of-the-art energy resolution in the full energy range (0.2 to 15 keV). The pixel size of 130 $\mu$m $\times$ 130 $\mu$m, corresponding to $2.23'' \times 2.23''$, is well matched to the expected performance of the mirror system (5″) HEW on-axis.

The measurement of the arrival time of the x-ray photon is determined by the anticipated read-out time of 5 ms. Since the required size of the large detector cannot be realized with the diameter of available ultrapure Si wafers, it is subdivided into four quadrants with $67 \times 67$ mm$^2$ each, leading to insensitive gaps between the quadrants. A workaround for this deficiency is using dithering observations of the sky region of interest. In total, $1024 \times 1024$ DEPFET pixels are placed on the full detector plane, resulting in $512 \times 512$ pixels per quadrant. Each quadrant is controlled independently by 8 Switcher-A ASICs and read out by eight Veritas-2 ASICs (for details of the electronic concept see Ref. 1). To derive a lower power consumption, the DEPFETs are operated in rolling shutter mode, which means: one DEPFET line is switched on while the others accumulate photons without power consumption. The Si-sensor has coatings on both sides. A 5-$\mu$m-thick benzocyclobutene layer on the off-mirror side is used for passivation. While a 90-nm-thick aluminum coating on the mirror side of the detector serves as an on-chip filter to reduce the contamination of the x-ray signal by optical light.

The large area imaging capability of WFI is complemented by the addition of a smaller $8.3 \times 8.3$ mm$^2$-sized fast timing detector, employing the same DEPFET technology. The so-called fast detector (FD) is placed beside the large detector and is defocused by $\sim$35 mm to allow for a high throughput during observations of bright sources of about 1 Crab intensity. The FD with $64 \times 64$ pixels is controlled and read out in two halves in parallel, thus improving the time resolution by a factor of two, such that the high time resolution requirement of 80 $\mu$s is fulfilled.

The LDA and FD, together with control and analog frontend electronics are surrounded by an aluminum shield, which is intended to reduce the proton flux to the detector to mitigate the radiation damage. With the planned thickness of 4-cm aluminum equivalent, the shield is able to stop, on average, protons up to $\sim$125 MeV.

As an outcome of the presented and previous studies (Ref. 2), a graded-Z shield will be mounted as an extralayer inside the proton shield to suppress aluminum-fluorescence radiation at $\sim$1.5 keV. In addition, it will reduce the contribution of secondary photons from primary proton interactions and Compton scattered primary hard x-rays. Much work has been done in the past to optimize the graded-Z shield to minimize the instrumental background due to secondary and primary electrons and photons (Ref. 2). Bringing together past and current background studies and a feasibility analysis, the current baseline for the graded-Z shield is 3 mm of molybdenum and on top 40 $\mu$m of polyimide (Kapton), with the polyimide facing toward the detector. The polyimide will most probably be glued to the molybdenum using an epoxy adhesive. This adhesive needs to be taken into account in background simulations as it will contribute to the suppression of fluorescence lines.

In addition to the previously described camera head, consisting of Si-detector, proton shield, and graded-Z shield, the WFI instrument has a filter wheel (FW) in front of the camera as well as an optical stray-light baffle. The FW allows one to move four different slots in front of the LDA. These slots contain a UV and visible light blocking filter, an open position for efficient evacuation of the FW and camera head, a closed position for sensor protection and instrumental background measurements, and a position that hosts the on-board calibration sources.

## 1.2 *Key Science Drivers for Requirements on Athena Background*

Key science objectives for the WFI have been identified within the framework of Athena's "Hot and Energetic Universe" science theme.[5] These objectives (see also Ref. 6) include, e.g., the search for the active galactic nuclei at redshifts 6 to 8, which will appear as very faint point sources in the anticipated multitiered WFI survey.[7] The same survey will also push the surface brightness sensitivity to detect the extended emission of the first galaxy groups, i.e., the first building blocks of the dark matter structure filled with hot gas at redshifts around 2.[8] In the nearby universe, WFI observations of the very low surface brightness regions in the outskirts of galaxy clusters will allow the determination of the physical processes dominating the injection

of nongravitational energy into the intracluster medium as well as its chemical abundances.[9] Achieving those and many more science objectives will rely fundamentally on a low and well-characterized background.

The WFI background requirement on the background intensity is divided between x-ray sky components, which dominate the background spectrum below ~2 keV, and particle components that emerge above. Most of the work done thus far within the WFI background group has concentrated on the latter, not because the former is of little consequence, but because at this time it is important to concentrate efforts on particle components.

The background requirements are driven by the WFI science goals. In general, x-ray sky requirements, such as those on the stray x-ray light, are critical to achieve much of the survey goals. The requirements on particle components are of great relevance for the characterization of cluster outskirts.

According to ESA's Athena Science Requirements Document,[10] the requirement on the intensity of the quiescent particle background is:

Athena shall achieve a (focused and not focused) non-x-ray background (NXB) for wide-field observations of $<5.5 \times 10^{-3}$ cts/cm$^2$/keV/s between 2 and 7 keV. The contribution by the nonfocused component corresponds to a reference model and flux of the galactic cosmic ray (GCR) component, defined as follows: 80% of the flux of the GCR model during solar minimum as described in Equations (1) and (2) with $\phi = 379.3$ MV, as presented in the document "Consolidation of the absolute level of the Galactic Cosmic Ray (GCR) protons spectrum".[11] In addition, it is specified in the requirements document that the focused background (particles transmitted through the mirror) shall be below $0.5 \times 10^{-3}$ cts/cm$^2$/keV/s. If the focused background level should amount to $0.5 \times 10^{-3}$ cts/cm$^2$/keV/s, the required not-focused background level is $<5 \times 10^{-3}$ cts/cm$^2$/keV/s. This requirement on the NXB should ensure that for, e.g., faint clusters or outskirts of clusters with low surface brightness spectral features at 6 keV or the Bremsstrahlung exponential cut-off can be determined. The NXB refers to events not registered as cosmic x-ray events (direct particles and secondaries), which fall in the x-ray band between 0.2 and 15 keV. The spectra of incoming particles (at solar minimum) and unfocused photons are shown in Fig. 1(b) and Fig. 2, respectively. For the presented studies, 80% of the solar minimum, and therefore cosmic ray maximum flux, is used.

## 2 Background Components

### 2.1 *Charged Particle Background*

In the following, we briefly discuss the components of the charged particle background, which depend only mildly on the final orbit of the satellite. The current baseline orbit for Athena is around the second Lagrangian point (L2) of the sun-earth system.

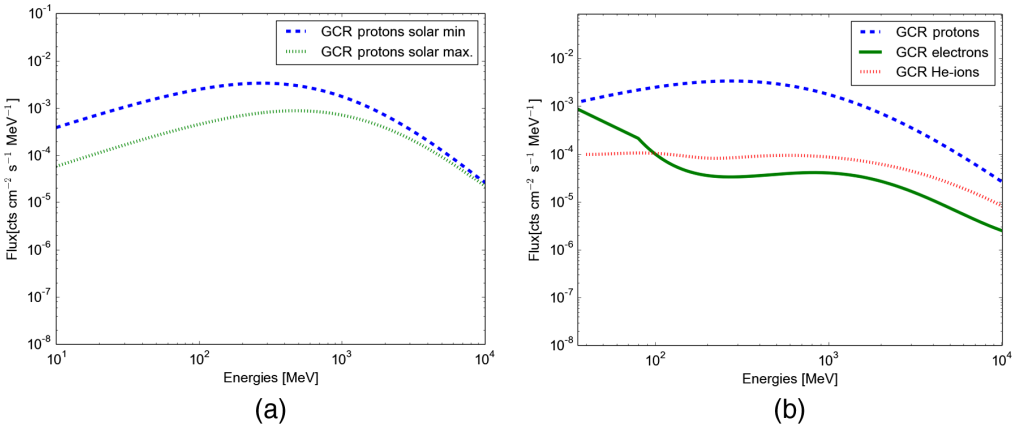


**Fig. 1** (a) The spectra of GCR protons at solar minimum and at solar maximum following Ref. 11. (b) The spectra of GCR protons,[11] electrons,[12] and He-ions[13] at solar minimum.

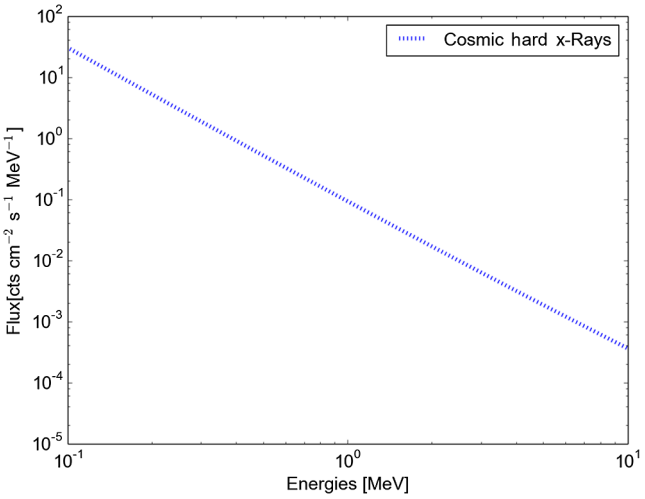


**Fig. 2** The spectrum of diffuse cosmic hard x-rays, as measured with HEAO-1.[14]

The charged particle environment of both L1 and L2 is composed of:

- GCR include protons, electrons, and He-ions with energies from several tens of MeV to several GeV. At the considered orbits, the GCR are subject to variations over the solar cycle. Here, low energetic particles vary more than high energetic ones, i.e., 200 MeV protons vary by more than a factor of two between solar maximum and minimum, whereas at 2 GeV this variation is only 10%, as visible in Fig. 1(a). The studies presented in this document use an updated spectrum for the galactic protons. This spectrum has been derived to give the most conservative estimate of the GCR proton spectrum and is based on data from Voyager2, SOHO, and PAMELA satellites and neutron monitor (NM) measurements. It is presented in Ref. 11.
- Two fits are applied to the PAMELA data in Ref. 11, one a conservative estimation for GCR proton fluxes at solar minimum and one a fit to the 2014 PAMELA data to estimate the GCR proton flux at solar maximum. Both resulting energy spectra are shown in Fig. 1(a). Spectra of GCR protons, electrons, and He-ions at solar minimum, as used in this publication, are shown in Fig. 1(b). Comparisons of the energy spectra of GCR He-ions and electrons, for different phases of the solar cycle, are shown in Refs. 15 and 16, respectively.
- Solar energetic particles (SEP) are mostly protons accelerated by the sun to up to 10 to 100 MeV. They are characterized by increases in the particle flux of several orders of magnitude.
- Suprathermal ions (STI) are mostly protons accelerated in the heliosphere to energies extending up to several hundreds keV. They vary significantly on time scales from a few seconds to hundreds of ks, potentially correlated with the solar cycle. At L2, an additional STI component from the Earth's magneto-tail is expected. Data accumulated over the last decades, while insufficient to provide a full characterization, indicate that the distant magneto-tail environment is highly structured with STI populating mostly, but not exclusively, the plasma sheet region. The limited data available suggest the plasma sheet should not intersect the large radius halo orbits around L2 proposed for Athena.

STI are akin to so-called soft protons (SP) encountered by XMM-Newton and Chandra on their High Earth Orbits. The difference between the two is that SP are mostly generated at Earth's bow shock, with a minor component associated with particles in free flowing solar wind, whereas, as previously mentioned, STI are mostly generated in the plasma sheet located in the magneto tail.

Both SEP and STI contribute to the concentrated particle background component. These are mostly protons concentrated by the Athena optics onto the focal plane. A magnetic diverter is

being designed to limit the impact of these particles on the WFI background. This study will concentrate on the GCR background.

### 2.2 *Cosmic X-Ray Background*

The cosmic x-ray background (CXB) is a diffuse radiation detected over the sky in a wide range of energies from extremely soft x-rays of about 0.1 keV to $\gamma$-rays above 1 MeV. It was discovered in 1962 and its precise origin remains puzzling. However, more recent observations, e.g., the deep surveys performed by ROSAT and Chandra satellites, show evidence that some fraction of the CXB is due to discrete sources (in fact more than 80% of the CXB has been resolved in the softer range up to several keVs). Below 3$\tilde{k}$eV, the CXB is primarily due to the hot galactic halo. Above 3 keV, the emission appears highly uniform and isotropic across the sky, suggesting that the bulk of the CXB has an extragalactic origin, though above 300 keV measurements are affected by systematic uncertainties larger than 20%. Above 3 keV, the CXB spectrum observed by HEAO-1 satellite[14] is remarkably close to the spectrum associated with thermal bremsstrahlung radiation with a temperature kT ~40 keV; at energies higher than 60 keV, the fit to the data requires the sum of three power laws. The cosmic x-ray spectrum is shown in Fig. 2.

### 2.3 *Production of Secondaries*

The incoming background particles (henceforth called primary particles) described in the previous section interact with the whole of the Athena instrument and produce secondary particles. Depending on the type, energy, and angular direction of these incoming primary and secondary particles, they might hit the detector and deposit energy in the detector. Energy depositions in the 2- to 7-keV energy band contribute substantially to the background for the wide-field observations. While the contributing secondary electrons are mainly generated in ionization processes, the secondary photons, apart from the fluorescence photons, are mainly generated by Bremsstrahlung and inelastic scattering processes.

## 3 Outline

The Monte Carlo simulation studies shown in this document are divided, according to their topic, into three different sections:

1. Geant4 shielding optimization studies are described in Sec. 4. These studies aim to find the best shielding configuration with respect to shielding layer thicknesses and shielding positions. The graded-Z shielding should lower the mean instrumental background level and reduce fluorescence lines in the energy range of the WFI.
2. An experimental verification of Geant4 simulations is presented in Sec. 5. The accuracy of simulations in the energy range of interest for the WFI has been studied, comparing lab experiments with simulations.
3. A description of the resulting WFI instrumental background is given in Sec. 6, once with and once without taking into account external masses.

## 4 Geant4 Shielding Optimization Studies

This section describes the different shielding optimization studies performed using Geant4/GRAS software. It starts with an outline of the input information necessary for performing Monte Carlo simulation studies. The Geant4/GRAS settings used in the simulations studies are described in Sec. 4.1, Sec. 4.2 presents the baseline simplified WFI mass model used as input for most simulation studies, and Sec. 4.3 presents the external masses used in the characterization of nearby masses. The second part of this section describes the simulation studies. The focus of these studies is the minimization of the anticipated background intensity. In addition, fluorescence lines in the WFI energy observation range should be prevented as far as possible. Special care has been taken to understand the systematic uncertainties due to variations of the WFI

design. To find the best graded-Z shield regarding the choice of materials and their thicknesses, a simplified box model has been used, as described in Sec. 4.4. In this way, many different configurations could be simulated in an acceptable time frame. The following Sec. 4.5 compares the remaining fluorescence counts for different shielding positions, using the optimized shielding composition found in Sec. 4.4.

### 4.1 *Geant4/GRAS as Tools to Derive the In-Flight Background*

The simulations presented in this document have been performed using Geant4:[3] a general-purpose Monte Carlo toolkit for elementary particles passing through and interacting with matter, originally designed for high energy particle physics. Geant4 is an open-source object-oriented simulation toolkit that offers a wide set of electromagnetic and hadronic physics models. It has good performance for the particle transport in complex geometry models and the possibility of interfacing to external packages such as simulation engines and visualization or analysis tools. An effort has been made to adapt Geant4 settings to space physics, for electromagnetic interactions a specialized physics list for space processes is used,[17] developed in the AREMBES effort (for AREMBES Geant4 validation see Refs. 18 and 19). Geant4 Radiation Analysis for Space (GRAS)[4] is a Geant4-based tool that deals with common radiation analyses types in generic three-dimensional models. Due to its modular design, ease of use, and flexibility, it is a convenient toolkit to simplify the usage of Geant4 for space applications. The Geant4 version used for the background studies presented in this paper is Geant4 10.03 together with GRAS version 04.00.

Geant4 simulates the path of one incoming primary particle, its energy deposition in matter, plus the possible generation of secondary particles and their subsequent interaction with matter. The energy deposited in the sensitive detector volume in adjacent pixels by one incoming primary and its secondaries, together with the particle rate of this type of primary particle background, is used to calculate the background rate.

The physics of different particle processes is included in Geant4 using physics lists. The physics list defines the particles, physics processes, and cut-off parameters for use in the simulation. Using physics lists allow the user to choose the best-suited physics models for the energy ranges and processes of interest, thus giving the user the freedom to trade physics accuracy versus computational speed. This freedom requires the user to have a good understanding of the underlying physics, as the omission of particles or physics processes could cause errors or poor simulation accuracy. The physics lists used for simulations described in this document are: QBBC, a physics list for hadronic processes, and the space user physics list. The QBBC list is a ready-made list of hadronic physics processes to be used for different particle and energy ranges. It contains the Fritiof (FTFP) model for high energies, the Bertini (BERT) model for intermediate energies, and the binary cascade model (BIC) for low energies. It also has a high precision (HP) model to simulate the interaction of slow neutrons. The space user physics list is a special physics list for an HP simulation of electromagnetic processes in space physics and has been developed in the AREMBES effort.[17]

An important parameter for the user of Geant4 is the particle production threshold known as the range cut. In Geant4 simulations, if a process occurs in which secondary particles could be produced, the range of each secondary is checked against the range cut. Apart from some exceptions, if the range of the secondary particle is smaller than the range cut it will not be produced and its kinetic energy deposited at the site of the interaction. This affects the number of low energy deposits at the detector as well as the position of energy deposits. Choosing a good range cut is a balancing act. It needs to be low enough to get the physics one interested. However, choosing it too low could lead to infrared divergence for some processes and a huge amount of CPU time would be needed for the simulation. The default range cut used in the presented simulations is 1.0 $\mu$m.

To simulate an isotropic particle flux, the primary particles in the simulations are assumed to be emitted from a spherical surface surrounding the WFI model, where, at every point, the specific intensity varies with $\alpha$, the angle from the normal, as $\cos(\alpha)$. This functional form can be derived from a consideration of the particle flux as a function of direction through a unit area on a sphere sitting in an isotropic particle flux. Integrating the flux $\phi$ emitted with a cosine angular

distribution over the entire surface $S$ of a sphere with radius $r$ yields the number of produced particles $N_r$ in a given time frame. A factor $f_N$ is used to normalize the simulated energy spectrum to the expected real-world energy spectrum:

$$f_N = \frac{N_r}{N_S} = \phi \cdot \frac{S}{4 \cdot N_S},$$

where $f_N$ is the normalization factor, $N_r$ is the number of expected primary particles, $N_S$ is the number of simulated primary particles, $\phi$ is the flux of primary incoming particles [particles/cm$^2$/s], and $S$ is the surface from which primary particles are emitted [cm$^2$].

### 4.2 *Baseline Simplified WFI Mass Model for Geant4 Simulations*

The baseline WFI simplified model (Figs. 3 and 4) used in the current simulations is derived from the WFI E00023277 computer aided design (CAD) model. This CAD model includes the LDA and the FD inside the 4-cm-thick aluminum proton shield, the thermal interface, the FW inside the primary structure, and baffle. No graded-Z shield is included in the baseline model. FASTRAD SW 3.9.4.[20] has been used to simplify the CAD model and translate it to the Geant4 compatible Geometry Definition Markup Language (GDML) format. Care has been taken to model the structures close to the LDA as accurately as possible.

### 4.3 *Description of External Masses*

The WFI camera is surrounded by several mechanical parts and structures also mounted on the Science Instrument Module (SIM). This distribution of external masses has to be taken into account in estimating the overall WFI NXB level, as secondaries can be excited from these structures, which could then reach the WFI detector. The most massive part is the X-IFU dewar, which will be mounted at a distance of 1 to 1.5 m from the WFI camera (Fig. 5). The dewar is made mainly of aluminum but has a quite complex structure and contains various components and elements, as well as a lot of empty space inside. Therefore, in the simulations, it has been

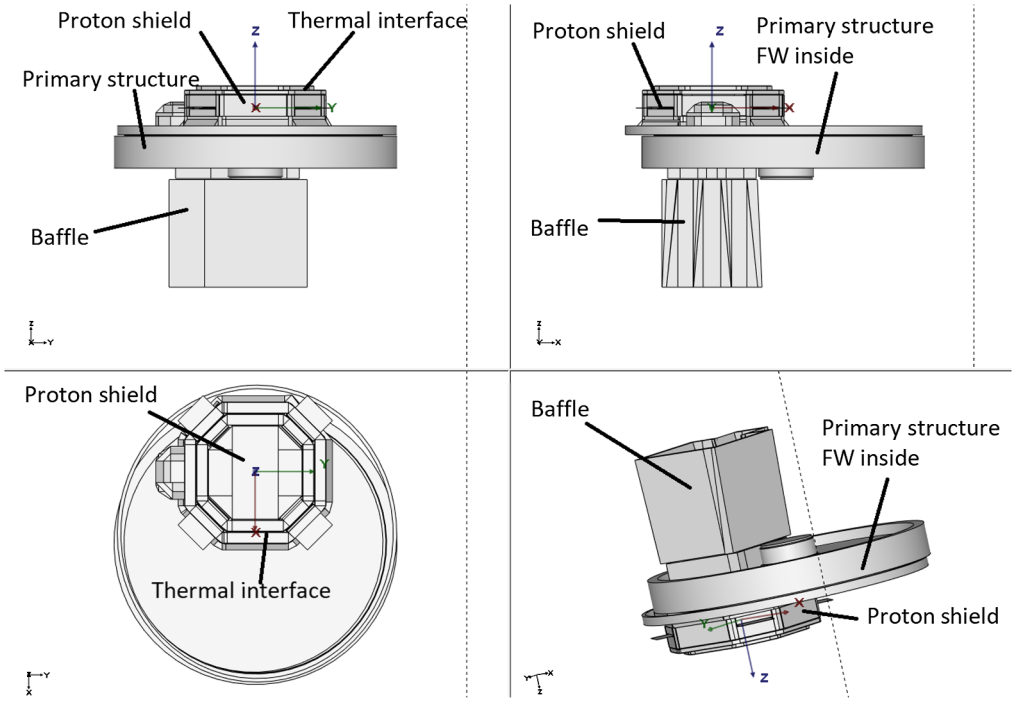


**Fig. 3** Simplified Athena WFI baseline model as used in Geant4 simulations in four different perspectives.

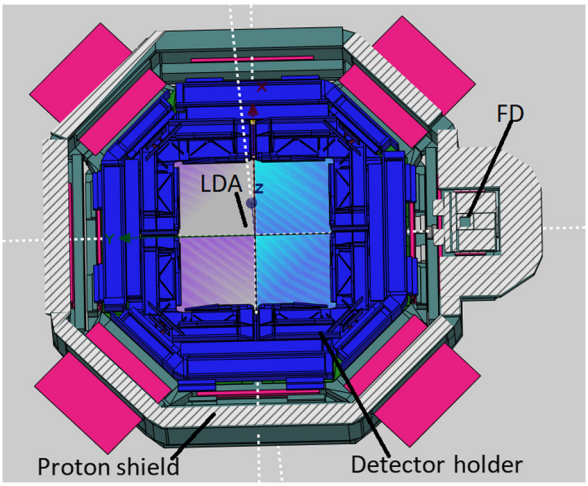


**Fig. 4** Cross-section in *x*-*y* plane through simplified baseline model of the camera head, showing the LDA and the FD as visible from the mirror-side of the detector. The shown colors are not naturalistic.

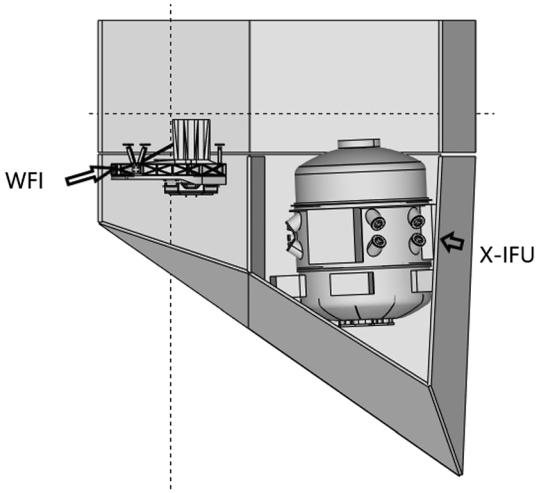


**Fig. 5** Schematic view of the WFI camera and X-IFU dewar on the SIM. The presented positions of WFI and X-IFU correspond the best knowledge at the time of the simulation studies and cannot be regarded as final positions.

modeled in a simplified way as a cylindrical volume, with an equivalent thickness of 70 mm and a height of 1300 mm. The equivalent thickness of aluminum has been estimated from the energy loss of protons passing through the dewar. We discuss in Sec. 6.2 the results of simulations and the impact of the X-IFU dewar on the WFI NXB level.

### 4.4 *Optimizing the Graded-Z Shield on Simplified Box Model*

The first phase of the study on the WFI NXB had led to the conclusion that an inner shield should be adopted inside the aluminum bulk shield. This would conveniently reduce the secondary emission from the bulk toward the detector as well as improve the bulk stopping power against environmental hard z-ray photons (see Ref. 2). At this stage, as a preliminary and tentative baseline, an inner shield consisting of a bilayer with 1-mm Mo and 1-mm polyether ether ketone (PEEK) was considered, being a good compromise between desired performance and realistic possibility of technical implementation. Nevertheless, the corresponding overall NXB level, as simulated using mass model E00015261, still was ∼30% higher than the requirement, also due to

the contribution from secondary emission from external masses (namely the X-IFU cryostat, see Sec. 4.3) around the WFI camera. To improve the configuration design, Geant4 (G4) simulations have been systematically run on a basic box model, which requires less computational power and time. In this model, the detector is surrounded by a box-like graded-Z shield, with inner and outer volumes similar to the WFI camera head. Then, the shield parameters are varied to explore different combinations. Finally, the verification and confirmation of the results are performed with a more complete and detailed mass model, just for those combinations showing some clear benefits in terms of NXB level.

In a first round of simulations, the baseline materials, aluminum, molybdenum, and PEEK have been assumed and just the variation of their thicknesses has been investigated. During this stage of the analysis, PEEK has been considered a prime candidate for the low Z layer. Technical feasibility considerations have, in a later stage, lead to Kapton as the prime candidate. As a first step, the thickness of molybdenum has been increased while keeping constant the thickness of PEEK, to assess how much reduction of the fraction of NXB induced by CXB could be achieved. The larger the molybdenum thickness, the higher the photon rate attenuation. On the other hand, if the molybdenum thickness becomes too large, secondary particle generation, excited by charged particles in the molybdenum, could overcompensate this effect. Also, the larger the molybdenum thickness, the larger the weight, which should be kept within a reasonable limit. For this reason, only three different cases have been investigated: 3-mm Mo, 5-mm Mo, and 7-mm Mo (plus 1 mm PEEK in all three cases). Simulations showed that some improvement of the overall NXB can be achieved, with 3-mm Mo and 5-mm Mo performing slightly better than 7-mm Mo (see Table 1).

As a second step, assuming a thickness of 3-mm Mo, the PEEK thickness has also been changed to see whether any further improvement could be achieved. Four cases have been investigated: 0.125, 0.25, 0.5, and 1.5 mm. Simulations showed that the thickness of PEEK is useful to suppress molybdenum fluorescence lines but does not significantly affect the continuum level. In fact, the mean values of NXB in the 2- to 7-keV range resulted quite similar to each other, within statistical errors, as reported in Table 2.

Similar simulations have been then repeated replacing PEEK with other possible alternative low-Z materials suitable for implementation, namely Kapton and polypropylene. Even in this case, the simulations indicated only minor differences, the three candidate materials behave in a similar way and can be considered interchangeable in terms of associated NXB. As an example, in Table 3, the relative variations are compared for a layer with a thickness of 0.125 mm.

Furthermore, a configuration with a reduced thickness of the aluminum bulk shielding (i.e., 30 mm instead of 40 mm) has been investigated as well since the proposed increase in the molybdenum layer thickness would offer an extra protection against radiation damage. A decreased aluminum thickness leads to more background induced by CXB and cosmic electrons. Reducing the aluminum thickness from 40 to 30 mm increases this background contribution by ∼20%. However, decreasing the aluminum thickness leads on the other hand to less background due to secondary particles induced by cosmic protons and He-ions, which compensates the CXB and

**Table 1** Summary of NXB relative variation (wrt. configuration 0) for different input particles and configurations. Configuration 0 = 40 mm Al + 1 mm Mo + 1 mm PEEK. Configuration 1 = 40 mm Al + 3 mm Mo + 1 mm PEEK. Configuration 2 = 40 mm Al + 5 mm Mo + 1 mm PEEK. Configuration 3 = 40 mm Al + 7 mm Mo + 1 mm PEEK.

| Input particle | Configuration 1 | Configuration 2 | Configuration 3 |
|---|---|---|---|
| GCR protons | $+2.7\% \pm 3.2\%$ | $+5.9\% \pm 4.2\%$ | $+8.8\% \pm 4.1\%$ |
| GCR He-ions | $-9.2\% \pm 5\%$ | $-11.5\% \pm 5.1\%$ | $-2.2\% \pm 5.1\%$ |
| GCR electrons | $-3.1\% \pm 7.4\%$ | $-8.2\% \pm 7.5\%$ | $-11.7\% \pm 7.9\%$ |
| CXB photons | $-67.3\% \pm 1.4\%$ | $-80.2\% \pm 1.1\%$ | $-85.8\% \pm 0.8\%$ |
| All primary particles | $-10.1\% \pm 3.7\%$ | $-10.5\% \pm 4.6\%$ | $-9.6\% \pm 4.6\%$ |

**Table 2** Summary of NXB relative variation (wrt. a configuration with 40 mm Al + 3 mm Mo w/o PEEK layer) for different thicknesses of the PEEK layer.

| PEEK thickness (nm) | NXB relative variation |
|---|---|
| 0.125 | $-7.2\% \pm 2.6\%$ |
| 0.25 | $-5.1\% \pm 2.6\%$ |
| 0.5 | $-3.5\% \pm 2.9\%$ |
| 1 | $-4.6\% \pm 2.9\%$ |
| 1.5 | $-2\% \pm 2.9\%$ |

**Table 3** Summary of NXB relative variation (wrt. a configuration with 40 mm Al + 3 mm Mo w/o low-Z layer) for a 0.125-mm layer of PEEK, Kapton, and polypropylene.

| Material (0.125 mm) | NXB relative variation |
|---|---|
| PEEK | $-7.2\% \pm 2.6\%$ |
| Kapton | $-6.5\% \pm 2.6\%$ |
| Polypropylene | $-8.9\% \pm 2.6\%$ |

cosmic electron contribution. It has been found that within errors both aluminum thicknesses, 30 and 40 mm, can be considered equivalent.

In conclusion, the findings of the study conducted on the basic mass model can be summarized as follows: increasing the thickness of the inner layer of Mo from 1 to 3 mm or 5 mm would allow to gain $\sim$20% reduction in the overall NXB. Even though in these simplified simulations, a thickness of 5-mm molybdenum seems to work slightly better than a thickness of 3 mm, the latter one could be preferable to keep the layer weight as low as possible; an increased thickness of the inner layer of molybdenum would also offer an extraprotection against radiation damage, which would allow to reduce then the thickness of the aluminum bulk shield from 40 to 30 mm without any significant impact on the overall NXB level. According to simulations, the composition and thickness of the inner low-Z layer does not affect significantly the overall continuum level. In this case, the choice of material thickness and composition could be driven by other properties of the material, e.g., mechanical stability, out-gassing, etc., provided that a low Z layer thickness sufficient to fully suppress the molybdenum fluorescence L-line is used.

### 4.5 *Effect of Varying the Shielding Positions on Fluorescence Photon Counts*

Three different shielding position configurations have been simulated.

- ID 0: Baseline configuration: A full graded-Z shielding inside of the camera head (3-mm Mo and 1-mm PEEK), and 1-mm PEEK shielding on the inside of beam path opening of the primary structure.
- ID 1: A full graded-Z shielding on the inside of the camera head but no other graded-Z shielding.
- ID 2: A full graded-Z shielding on the inside of the camera head and 1-mm PEEK shielding on the inside of the WFI baffle walls, no shielding on the inside of the beam path opening of the primary structure.

The position of the different parts of the WFI is marked in Fig. 3. For the baffle and instrument structure, no molybdenum shielding has been considered for the following reasons:

1. The aluminum layer of the instrument structure surrounding the detector opening is thin (a few mm); therefore, the number of Bremsstrahlung photons generated in this layer should be few. Adding a molybdenum layer would lead to more Bremsstrahlung photons and hence background.
2. An additional molybdenum layer on these thin parts would increase the overall weight of these extended components and could critically affect the structural integrity of the WFI.

The resulting aluminum K line photon background hits and molybdenum L photon background hits are presented in Table 4. The lowest amount of aluminum line photon background hits can be observed with the baseline shielding configuration ID 0. Further reduction to $\sim 0.3 \pm 0.1$ counts/cm$^2$/s would be possible if, in addition to the ID 0 shielding, the baffle walls could be shielded with a low Z material. This number has been estimated by subtracting from the aluminum K line photon counts, photons emitted from the baffle walls. The technical feasibility of shielding the baffle walls is currently under discussion. Also, for the reduction of molybdenum L line photons, shielding configuration ID 0 is the best choice of the three. Only very few molybdenum L line photons remain. The origin of aluminum L line photons and molybdenum K line photons for shielding configuration ID 1 is shown in Fig. 6. The majority of the aluminum K line photons originates from the primary structure and the FW. This is due to an incomplete low Z shielding of these structures. The overall aluminum count could therefore be further reduced, if a complete low Z shielding of these structures would be possible. The majority of the molybdenum L line fluorescence photons originates from the detector holder, directly adjacent to the detector. Attaching a low Z shielding here is particularly difficult due to thermal stress and the closeness of the detector. The detector holder will be cooled together with the detector, and this would induce thermal stress into a low Z layer attached to the inside of the detector holder. To reduce risks to the detector, a low Z layer on the inside of the detector holder is therefore not foreseen and also according to the simulations not strictly necessary.

**Table 4** Aluminum K and molybdenum L line fluorescence photon hits.

| Shielding configuration | Aluminum K photons $\cdot 10^{-3}$ [counts/cm$^2$/s] | Molybdenum L photons $\cdot 10^{-3}$ [counts/cm$^2$/s] |
|---|---|---|
| ID 0 | $0.7 \pm 0.1$ | $0.3 \pm 0.1$ |
| ID 1 | $2.5 \pm 0.1$ | $0.6 \pm 0.1$ |
| ID 2 | $2.0 \pm 0.1$ | $0.5 \pm 0.1$ |

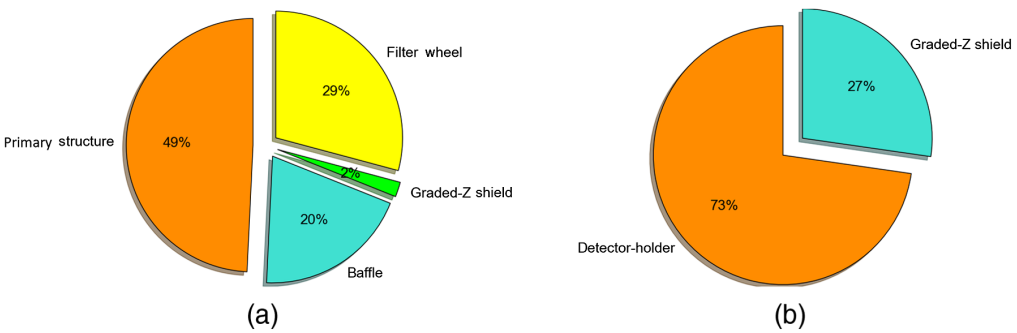


**Fig. 6** Origin of fluorescence photons hitting the detector for shielding configuration ID 1. (a) The origin of aluminum K line photons and (b) the origin of molybdenum L line photons.

## 5 Experimental Verification of Geant4 Simulations

Significant efforts have been made within the Athena WFI Background Group to validate the physics processes within the Geant4 simulation toolkit. Specifically, for the application to instrument background generation relevant to radiation which will impact images produced by the WFI. Previous research in this area has focused on validating Geant4's simulation of particles that are well above the energies that will influence the background within the WFI.[21–24] The off-axis x-ray-like background experienced by the WFI is expected to be primarily generated by secondary particles between several keVs and several hundred keVs and therefore requires specific and additional focus.

Therefore, three phases of experiments have been performed to assess the accuracy of Geant4 simulations within the context of low energy background-inducing particles in the space-based environment.[25] Initial proof-of-concept and test phases, phases I and II, were performed at the Synergy Health proton facility, Oxfordshire, United Kingdom, using 6 MeV protons, whereas phase III was performed at the Proton Irradiation Facility (PIF) at the Paul Scherrer Institut (PSI), Aargau, Switzerland, using 200 MeV protons to better represent the space environment. Corresponding simulations were developed for each of the experimental campaigns to validate Geant4's abilities to simulate x-ray-like background. Here, we report on the results of the phase III experiment, which is the most relevant for the Athena WFI.

### 5.1 *Experimental Setup*

An experimental chamber was designed as shown in Fig. 7. The chamber was oriented such that protons from the PIF beamline would pass through a 2.8-cm-thick plate of aluminum at 45 deg to the surface normal such that the thickness of aluminum traversed by the beam was 4 cm, followed by two 1-mm-thick targets also at 45 deg to the beamline. The detector plane is perpendicular to the direction of the incoming protons such that the detector views the target perpendicular to the incoming proton beam. The detector sees the single surface of the target material stack, for example, seeing the low Z layer (beryllium) only in the Al-Mo-Be case, albeit with the protons passing first through the aluminum layer, then the molybdenum layer and finally the beryllium layer. The detector will also see the inside of the chamber between the detector plane and the target, but this additional material is included within the simulation and the incident proton beam itself does not interact with the chamber wall. Secondary particles

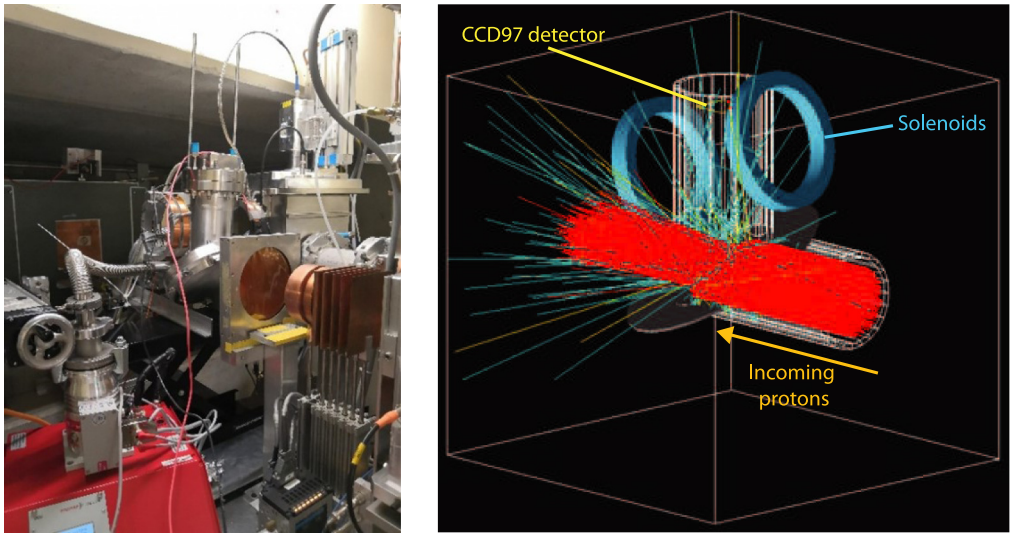


**Fig. 7** (a) An image of the experimental chamber positioned in the beamline at the PSI PIF and (b) the equivalent simulated geometry. The solenoids were used as part of the experimental program to allow deflection of the soft electron secondaries.

**Table 5** The material configurations that were irradiated in phase III tests at the PSI PIF. As the aluminum and target material layers were oriented at 45 deg to the beamline, the thickness traversed in each layer is equal to the actual thickness of the layer multiplied by the square root of 2.

| Configuration | Thickness traversed by protons |
|---|---|
| Aluminum only, no graded-Z sample | 4 cm Al |
| Aluminum → molybdenum | 4 cm Al → 1.414 mm Mo |
| Aluminum → molybdenum → beryllium | 4 cm Al → 1.414 mm Mo → 1.414 mm Be |
| Aluminum → molybdenum → PEEK | 4 cm Al → 1.414 mm Mo → 1.414 mm PEEK |
| Aluminum → tungsten → PEEK | 4 cm Al → 1.414 mm W → 1.414 mm PEEK |

generated by protons passing through the shield materials would then be observed by the detector without the detector being subjected to the primary beam. This geometry was designed to emulate the structure of material a cosmic proton might pass through in the space-based environment of the WFI (several centimeters of aluminum proton shield followed by two thin graded-Z shielding layers).

Five irradiations were performed using different combinations of materials for the target, which are given in Table 5. These configurations were chosen to represent candidate materials at the time of the experiment for the WFI graded-Z shielding.

At the time of the experiment, PEEK was one of several shortlisted materials under discussion for the baseline configuration for the low-Z shielding layer. However, the graded-Z shield is now expected to be composed of a molybdenum high-Z layer and a Kapton low-Z layer. Within the limitations of the materials simulated, other simulations have demonstrated that the choice of the low Z layer does not significantly alter the background, other than modifying the effectiveness at attenuating fluorescence lines.[2] Therefore, it is not expected that the results for the actual graded-Z shielding configuration will significantly differ from the configurations with two shielding layers given here. Although, this needs to be confirmed by further test campaigns in the near future.

The detector used in the experiment was a CCD97,[26] an EMCCD with an ∼14-$\mu$m-thick-sensitive region[27] and $512 \times 512$ pixels of width 16 $\mu$m. While this detector has a sensitive region that is significantly thinner than the WFI DEPFET sensitive region of 450 $\mu$m, it is still suitable for investigating a key component of the background: the secondary soft-electrons generated when a proton passes through the innermost surfaces of the shielding materials[2,28] as well as the fluorescence in the WFI energy band. Future experiments at the PSI PIF that are currently scheduled will use a detector with a thickness more comparable to the WFI DEPFETs, to test the current baseline molybdenum-Kapton graded-Z shielding configuration.

Simulations used Geant4 10.4.p01 with the corresponding version of the Space Users Physics List[17] built onto QBBC, with a cut length of 1 $\mu$m. Fluorescence, Auger electrons, and particle-induced x-ray emission options were also all turned on, as was single scattering, and the minimum energy was set to 100 eV. The CCD97 was modeled as a single 14-$\mu$m cuboidal block of silicon. Energy depositions in the silicon were recorded and pixelated into images, and event detection algorithms were applied to convert images to spectra.

## 5.2 *Results*

A selection of the total experimental and simulated energy deposition spectra for the irradiations are displayed in Fig. 8. Figure 8(a) displays several of the simulation spectra plotted with the Al → Mo experimental spectrum, showing that there is little variation in the general shape of the experimental spectrum with respect to material configuration. The Geant4 spectra also appear to be in good agreement with the experimental spectra above ∼5 keV. It should be noted that the aluminum 1.49 keV fluorescence line appears in all experimental runs due to the aluminum structure of the main experimental chamber, acting as a secondary energy calibration.

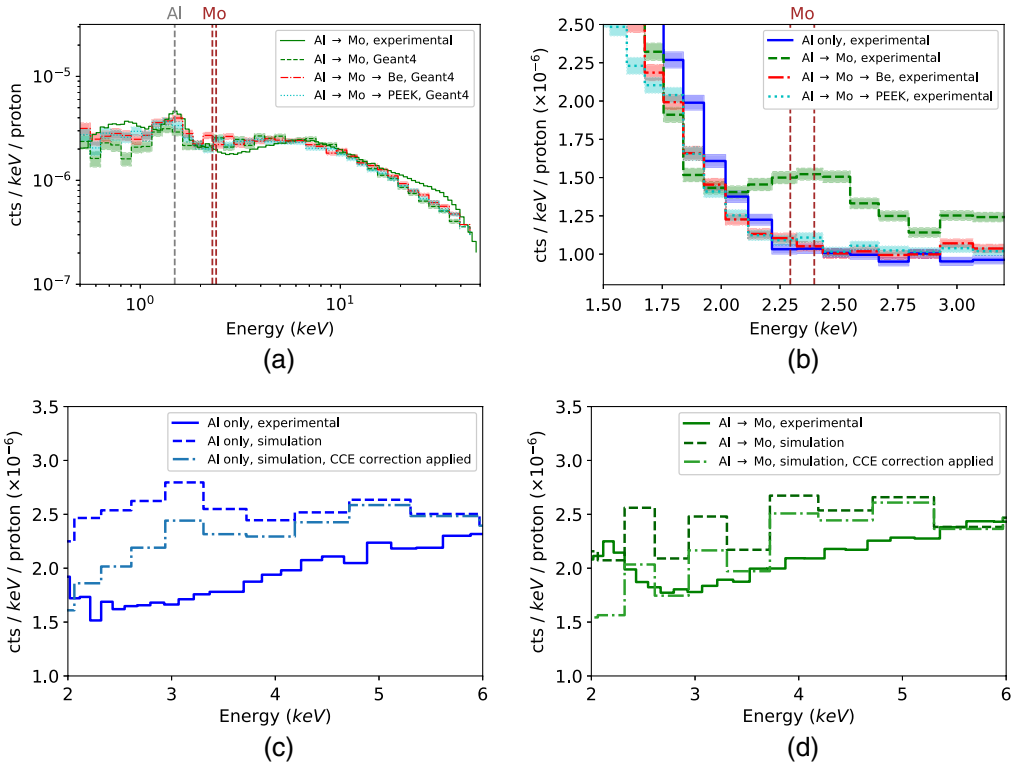


**Fig. 8** Experimental and simulated spectra from 200 MeV proton irradiations at the PSI PIF. (a) The total energy deposition spectra for several material combinations and (b) the spectra for several configurations around the region of the 2.3 and 2.4 keV molybdenum fluorescence lines when the solenoids in the experiment were switched on. (c) and (d) Spectra for the aluminum only and aluminum → molybdenum configurations between 2 and 6 keV, and the effectiveness of CCE corrections at reducing discrepancies between Geant4 and experimental spectra.

There does however appear to be some divergence between the raw simulated data and that found in the experimental testing between ∼2 and 5 keV in energy. As a worst case, the Geant4 simulations would appear to overestimate the electron continuum spectra by up to 50%. However, further analysis suggests that this is due, at least in the most part, to incomplete charge collection at the back surface of the CCD in the experimental data. Using data from experiments that were performed at Berliner Elektronenspeicherring-Gesellschaft für Synchrotronstrahlung (BESSY) in Berlin on a CCD97,[29] a correction to simulate the incomplete charge collection at these lower energies in the experiment was applied to simulated data to give the spectra shown in Figs. 8(c) and 8(d).

The application of this charge collection efficiency (CCE) correction improves the agreement between simulation and experimental data between 2 and 5 keV, and although it does not entirely account for the discrepancy, leaves an uncertainty related to the validity of the simulated spectra over the 2 to 7 keV energy band of ∼20% when including all experimental errors. The next experimental campaign will aim to examine this discrepancy in further detail, particularly with regard to the variation between shielding candidates.

Additional discrepancies are seen at around 0.8 and 35 keV. These discrepancies are outside of the key 2 to 7 keV energy band of greatest interest for the Athena WFI instrumental background and therefore were not studied in greater detail within this study. However, it should be noted that they fall at the outer edges of the capabilities of the technique due to detector noise and detector thickness (QE), respectively, and therefore further device-specific simulations would be required to analyze any discrepancy further.

In addition to verifying the accuracy of Geant4 at simulating x-ray-like background induced by secondary particles, this experiment was also able to assess the effectiveness of graded-Z shielding at removing fluorescence lines from the background. Several solenoids were placed around the detector in a Helmholtz coil structure such that when a current was passed through the solenoids,

secondary electrons would be magnetically diverted away from the detector leaving the photonic components to dominate the resulting spectra. This meant that fluorescence from molybdenum previously obscured by the electron continuum could be exposed, and the resulting spectrum when the magnetic field was switched on is displayed in Fig. 8(b). The fluorescence lines from molybdenum only appear in the aluminum and molybdenum only spectrum and is absent in spectra that include the beryllium and PEEK. This indicates that beryllium and PEEK are successfully attenuating the molybdenum 2.3 and 2.4 keV fluorescence lines, as one would rightfully expect.

### 5.3 *Future Experiments*

The results for this experiment are promising and indicate that Geant4 is capable of providing secondary particle spectra estimates accurate over a wide range of energies. To further validate the use of Geant4 at simulating the x-ray-like background in the Athena WFI, another round of testing will be performed at the PSI PIF, where the CCD97 will be replaced with a 500-$\mu$m-thick AdvaPIX TPX3 detector[30] to better reflect the thickness of the WFI DEPFETs. The baseline graded-Z shielding configuration of a molybdenum high-Z layer with a Kapton low-Z layer will also be used in the next round of testing.

## 6 Simulated WFI Background with Optimized Baseline Model

### 6.1 *Background Simulation Without External Masses*

Using the outcome of the graded-Z shield studies, presented in Sec 4.4 and Sec. 4.5 and the results of previous studies,[2] the following changes have been made to the baseline WFI model presented in Sec. 4.2. The proton shield in the optimized model has been reduced from 4 to 3 cm thickness. To compensate for the resulting loss in radiation protection and to suppress secondary and primary photons, a 3-mm-thick Molybdenum layer together with 1 mm of PEEK are included as a graded-Z shield inside of the proton shield, following the ID 0 shielding configuration description in Sec. 4.5. The low Z PEEK layer suppresses the resulting aluminum and molybdenum fluorescence lines. In the new baseline shielding model, the inside of the detector opening in the FW and instrument structure are as well coated by 1 mm of PEEK. The low Z PEEK layer, used in the Geant4 simulations described in this section, stands in contrast to the low Z Kapton layer described in Sec. 1.1. This is due to the fact that the graded-Z shield composition described in Sec. 1.1 is an outcome of these simulations plus a technical feasibility study.

The resulting background is presented in Fig. 9. The different shape of background due to cosmic hard x-ray photons and cosmic particles is clearly visible. While the particle background is relatively flat in the regarded energy range, the photon background increases with decreasing energy. This is confirmed in Table 6, which presents the best-fitting parameters of first-order polynomials for the particle background spectra and a second-order polynomial for the photon background spectra. A chi2 criteria has been used to find the appropriate polynomial degree for the different background spectra. Figure 9 shows that the aluminum K alpha line is visible both in the proton as well as in the He-ion spectrum. This distinguishes the deviation at the energy of the aluminum K alpha line from other positive or negative deviations visible in Fig. 9.

The mean background level between 2 and 7 keV is presented in Table 7, in the first column without any additional software rejection algorithms, in the second column all hits touching the detector borders have been excluded and in the third column, a 20% margin has been added to the mean background level to account for simulation uncertainties. Removing hits touching the detector border lowers the overall background level. Next to the detector border, energy might be lost; in this case high energy hits might lose enough energy to be recorded in the energy band of the WFI. Without further cleaning processes, the background is not compatible with the requirement stated in Sec. 1.2.

Figure 10 shows on the left-hand side the fractional background contributions of the main primary particles and on the right-hand side the fractional background contributions of particles impinging on the detectors. Galactic cosmic protons contribute approximately three quarters of the background, the rest is split almost evenly among cosmic He-ions, cosmic electrons, and

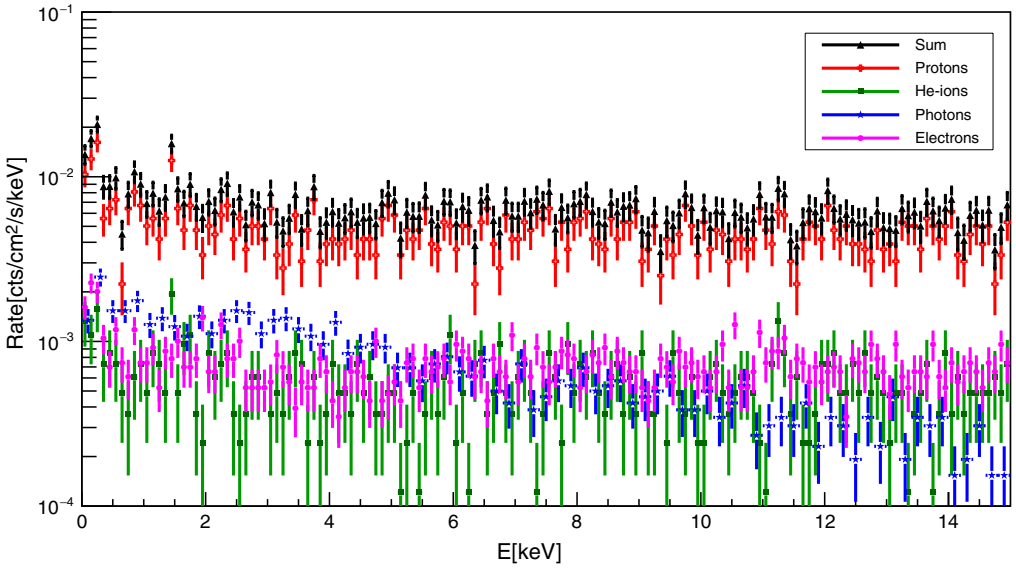


**Fig. 9** Instrumental background spectra due to cosmic protons (red), electrons (magenta), He-ions (green), photons (blue), and the sum of all (black). The simulation results were derived for the proposed optimized WFI configuration, including a Mo/PEEK graded-Z shield. No rejection algorithms have been employed.

**Table 6** Polynomial coefficients of a first-order polynomial fit to the different particle background curves and a second-order polynomial fit to the cosmic photon background. The chosen fitting region is 2 to 15 keV.

| Primary particle | p0 · $10^{-3}$ [cts/cm$^2$/s/keV] | p1 · $10^{-3}$ [cts/cm$^2$/s/keV$^2$] | p2 · $10^{-3}$ [cts/cm$^2$/s/keV$^3$] |
|---|---|---|---|
| GCR protons | $4.8 \pm 0.1$ | $-0.02 + -0.02$ | — |
| GCR He-ions | $0.43 + -0.04$ | $-0.003 + -0.004$ | — |
| GCR electrons | $0.58 + -0.04$ | $0.007 + -0.004$ | — |
| GR photons | $0.83 + -0.06$ | $-0.10 + -0.01$ | $0.0037 + -0.0007$ |

**Table 7** The mean simulated particle background level between 2 and 7 keV for different incoming particles in counts/s/cm$^2$/keV. The first row shows the full uncleaned background, the second row the background if hits touching the detector border are removed, the third row adds a safety margin to the background after the first cleaning.

| Primary particle | Mean Bkgd. · $10^{-3}$ [cts/cm$^2$/s/keV] | Mean Bkgd. excl. border hits · $10^{-3}$ [cts/cm$^2$/s/keV] | Mean Bkgd. excl. border hits + syst. unc. · $10^{-3}$ [cts/cm$^2$/s/keV] |
|---|---|---|---|
| GCR protons | $4.81 \pm 0.08$ | $4.68 \pm 0.08$ | $5.62 \pm 0.08$ |
| GCR He-ions | $0.49 \pm 0.03$ | $0.49 \pm 0.03$ | $0.59 \pm 0.03$ |
| GCR electrons | $0.66 \pm 0.02$ | $0.64 \pm 0.02$ | $0.77 \pm 0.02$ |
| GCR photons | $0.48 \pm 0.02$ | $0.48 \pm 0.02$ | $0.58 \pm 0.02$ |
| Total | $6.44 \pm 0.09$ | $6.29 \pm 0.09$ | $7.54 \pm 0.09$ |

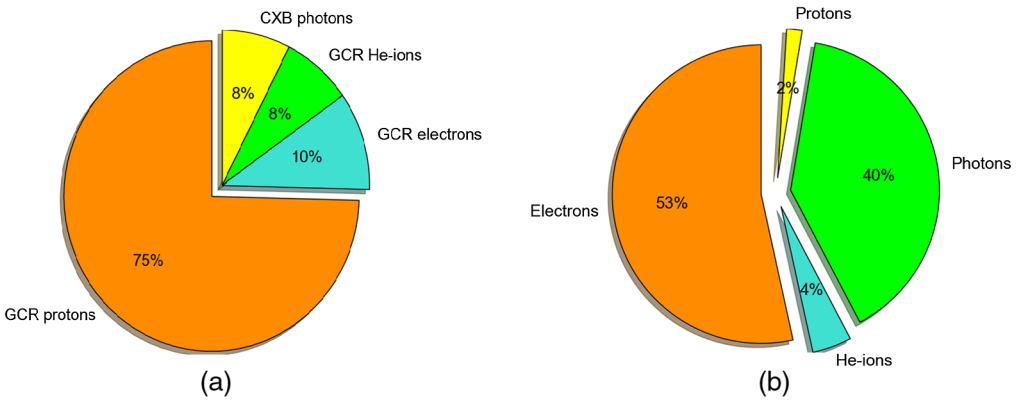


**Fig. 10** Fractional contribution to mean background level between 2 and 7 keV: (a) split according to the primary particle species and (b) split according to the particles species hitting the detector.

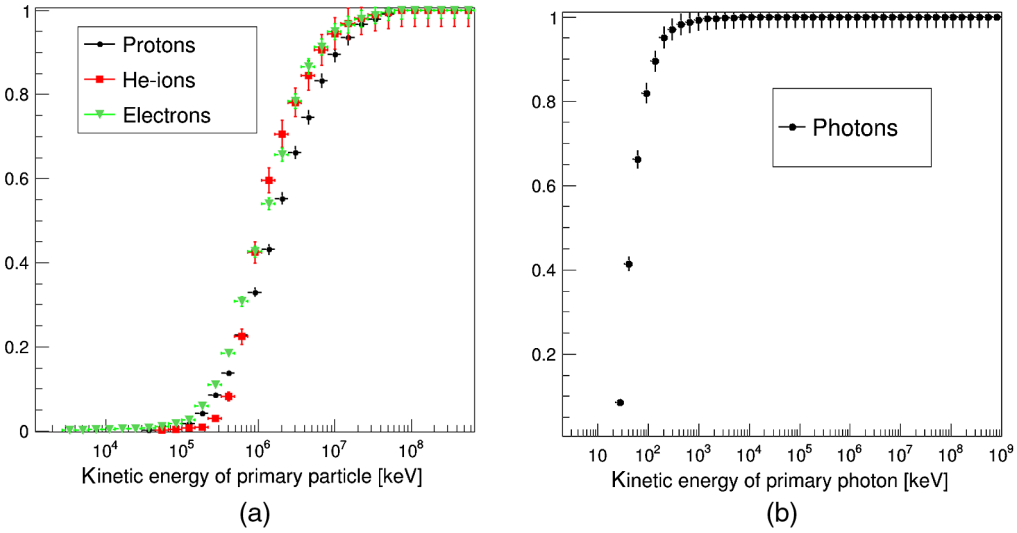


**Fig. 11** Cumulative distribution of the kinetic energy of (a) GCR particles and (b) CXB photons contributing to the instrumental background.

cosmic unfocused photons. The background is mainly generated by electrons and photons impinging on the WFI large detector-array.

Figure 11 shows the cumulative energy distribution of GCR particles (a) and CXB photons and (b) contributing to the instrumental background. It allows an estimation of how the background might change if the energy distribution of GCR particles and CXB photons changes. It indicates, for example, that an increase in GCR particles with energies below 100 MeV will likely not affect the background level. In contrast, primary particles with kinetic energies between ~100 MeV and 10 GeV and primary CXB photons with kinetic energies between 10 keV and 1 MeV have the highest impact on the instrumental background level.

## 6.2 *Background Estimation Including External Masses*

This assessment mainly concerns the impact of the presence of the X-IFU dewar, which is the most massive structure in the vicinity of the WFI camera, on the NXB level expected for the WFI detector and was initially conducted using mass model E00015261.[2] The dewar has been modeled in a simplified way as equivalent to a cylinder made of aluminum with inner radius 400 mm, outer radius 470 mm, and height 1300 mm. Simulations have been run for all primary particles both with and without dewar. The comparison showed that the presence of the dewar introduces an additional radiative component in form of secondary gamma rays, which are generated as a

**Table 8** Summary of NXB mean variation in 2 to 7 keV for different input particles mainly induced by secondary gamma rays in a configuration including the WFI mass model E00023277 plus the X-IFU dewar, relative to the NXB simulated for the mass model E00023277 w/o dewar.

| Input particle | NXB mean variation |
|---|---|
| GCR protons | $+6.1\% \pm 3.2\%$ |
| GCR He-ions | $+18.4\% \pm 10.1\%$ |
| GCR electrons | $+4.9\% \pm 3.7\%$ |
| CXB photons | $-9.6\% \pm 9.9\%$ |
| All primary particles | $+5.9\% \pm 4.3\%$ |

consequence of hadronic interactions of primary charged particles in the dewar mass. These gamma rays leave the dewar and have enough energy to penetrate through the aluminum bulk shield of WFI and reach the detector, where they do contribute to the NXB via Compton scattering. While all charged particles excite secondaries in the dewar mass and generate some additional emission (mostly stopped by the aluminum bulk shield), for CXB photons the presence of the dewar has just the effect of reducing the solid angle and preventing a fraction of the incoming flux from reaching the detector. The NXB variation, associated with the dewar in the mass model version E00015261, increased the overall background level by $12.3\% \pm 6.7\%$.

Similar simulations were then repeated following the evolution of the WFI camera design as well as the SIM design. In Table 8, we report quantitatively the relative variation of NXB for each type of primary input particle simulated using the latest mass model version E00023277, where the shielding structure consists of 30 mm Al + 3 mm Mo + 1 mm PEEK. According to an updated SIM design, with respect to former simulations, the distance between the dewar and the WFI detector has been increased from 1.1 to 1.4 m (see Fig. 5).

Although the shielding composition is not the only difference between the mass models E00015261 and E00023277, it is reasonable that the increased thickness of the molybdenum layer from 1 to 3 mm together with the larger distance between the WFI camera and the dewar more than compensate the reduction of thickness of the Al bulk shield from 40 to 30 mm. This then results in a lower additional NXB from the dewar for the mass model E00023277. It is worth stressing that the additional NXB is mainly associated with secondary energetic gammas, which can easily penetrate through a thin low-Z layer. Therefore, we expect that replacing PEEK with a different low-$Z$ material (e.g., Kapton) in the same E00023277 mass model version does not have a significant impact on the result.

The overall background level is given in Table 9, including the removal of hits touching the detector border, the inclusion of the effect of external masses such as the X-IFU dewar and taking into account systematic uncertainties on the Geant4 simulation process. These systematic uncertainties have been estimated to be about 20%.

Recently, eROSITA, an x-ray astronomical telescope also flying in L2, reported about a factor 2 higher background than expected by MC simulations.[31] Studies to understand this discrepancy are in progress. Care will be taken to understand if whatever caused the discrepancy will also affect the WFI background level. This might be for example an incomplete modeling of the external masses surrounding the eROSITA camera.

### 6.3 *Technical Feasibility of Graded-Z Shielding*

The graded-Z shield studies presented in the previous sections assumed that the lower Z layer would consist of 1 mm of PEEK. Regarding the technical feasibility, with respect to out-gassing, stability, availability, and thermal requirements, the choice of a suitable lower Z layer is much more limited. The current best choice of a lower Z layer would be, as stated in Sec. 1.1, 40 $\mu$m of Kapton glued with epoxy adhesive to the molybdenum high Z-layer. The foreseen Kapton is the

**Table 9** The mean simulated particle background level between 2 and 7 keV for different incoming particles in counts/s/cm$^2$/keV. The second column shows the background after removal of hits touching the detector border and taking into account external masses. Statistical errors correspond to the 1$\sigma$ error on the mean, systematic error account for a 20% uncertainty in the modeling of the WFI and surrounding and for uncertainties inherent in Geant4 simulations.

| Primary particle | Mean Bkgd. – border hits + external masses $10^{-3}$ [cts/cm$^2$/s/keV] |
|---|---|
| GCR protons | $4.97 \pm 0.08$ (stat) $\pm 1.0$ (syst) |
| GCR He-ions | $0.58 \pm 0.03$ (stat) $\pm 0.1$ (syst) |
| GCR electrons | $0.67 \pm 0.02$ (stat) $\pm 0.1$ (syst) |
| GCR photons | $0.45 \pm 0.02$ (stat) $\pm 0.09$ (syst) |
| Total | $6.7 \pm 0.1$ (stat) $\pm 1.3$ (syst) |

**Table 10** Molybdenum L line fluorescence photon hits for different thicknesses of a low Z layer and a possible adhesive thickness using a simple box model simulation.

| Shielding configuration | Molybdenum K photons $\cdot 10^{-5}$ [cts/cm$^2$/s] |
|---|---|
| 80 $\mu$m Kapton | 4.6 |
| 125 $\mu$m Kapton | 1.0 |
| 250 $\mu$m Kapton | 0.01 |
| 40 $\mu$m Kapton | 0.9 |
| 100 $\mu$m epoxy | — |

material with the maximum available thickness, which fulfills the required standards in outgassing, stability, positive thermal influence, grounding, and space qualification. Simplified background simulations have been used to estimate if this thickness suppresses sufficiently the molybdenum K line. In these simulations, an epoxy thickness of 100 $\mu$m has been assumed, which is in accordance with standard epoxy thicknesses for similar applications. The resulting molybdenum K line photon count should be in the same order of magnitude as that stated in Table 4 for ID 0. Using a 3-cm aluminum, 3-mm molybdenum box model (from outside to inside), with inner and outer volumes similar to the WFI camera head, the unsuppressed number of molybdenum L line photons has been estimated. Together with the transmission efficiencies for polyimide and polyether (Ref. 32), the remaining molybdenum K line photons have been calculated for several low Z layer variations (Table 10). All estimated remaining molybdenum K photon counts are one order of magnitude lower than those expected for shielding configuration ID 0, which are mainly emitted from the molybdenum detector holder. A change from the 1-mm PEEK thickness in shielding ID 0 to 40 $\mu$m of Kapton glued with about 100$\mu$ m epoxy should therefore have negligible effects on the overall expected molybdenum K line photon count.

## 6.4 *Effectivity of Rejection Algorithms*

As pointed out above, further reduction of the background level can be achieved through software rejection. To reduce the remaining background, several analysis strategies have been tested.

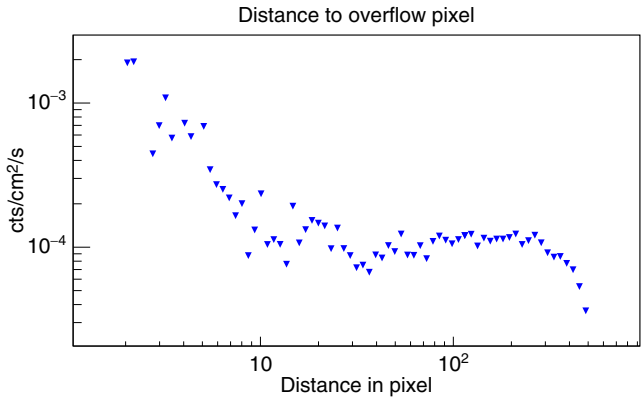


**Fig. 12** Smallest distance between background hit and overflow pixel given in number of pixel for galactic cosmic protons as primary particles.

One of them is the exclusion of hits, which are next to a pixel in which more than 15 keV of energy have been deposited (overflow pixel) during one integration time. The reasoning behind this threshold is that energy deposits above 15 keV are much more likely to originate from high energetic particles than from x-ray photons, which have been focused by the mirror onto the detector. Secondary particles produced by such a high energetic primary tend to hit the detector close to the primary that produced them. This is especially true if the secondaries are produced on a surface parallel and close to the detector. The closest distance between a background hit and an overflow pixel is depicted in Fig. 12 for GCR protons only. Two separate distributions can be seen, one peaking at small distances and one almost flat reaching up to large distances. The current assumption is that the first distribution is due to secondaries produced on a surface close and parallel to the detector, whereas the second distribution is due to secondaries produced further away from the detector or from secondaries due to unrelated primaries arriving during the same frame time. It is important to understand that this technique is limited to frames in which more than one hit has been detected. An in depth discussion of software rejection algorithms can be found in Ref. 33. Reference 33 studies especially the cumulative probability that a valid event falls within a certain radius of a particle track resulting from the same cosmic ray interaction. It finds that at the largest exclusion radius this probability reaches 35%. This could be regarded as the maximum amount of effective background improvement possible with the presented method.

## 7 WFI Background Summary

An extensive discussion of the WFI instrumental background and possible design changes to minimize this background have been presented. In addition, an experimental verification of the applicability of Geant4 simulations for energies and particles relevant for the Athena WFI instrumental background has been performed. The overall not-focused background level has been shown in Table 9. Including external masses such as the X-IFU and systematic uncertainties it is about 60% higher than the minimal required not-focused, NXB level given in Sec. 1.2. Based on in depth simulation studies we conclude that this is the best not-focused, NXB level achievable for the WFI DEPFET detectors at L2, if no further software rejection algorithms are employed. In Ref. 33 possible software rejection algorithms are discussed. The goal is to find rejection algorithms that optimizes the overall signal over background level.

## Acknowledgments

The authors are grateful to the whole Athena WFI project team and all colleagues, who contributed to the development or tests from the Max-Planck-Institut für extraterrestrische Physik (MPE), from the MPI HLL, in particular Danilo Mießner, and all others taking part in the project. This work was supported by the Max-Planck-Society and the German Aerospace Center (DLR).

## References


1. N. Meidinger et al., "Development status of the wide field imager instrument for Athena," *Proc. SPIE* **11444**, 114440T (2020).
2. A. von Kienlin et al., "Evaluation of the ATHENA/WFI instrumental background," *Proc. SPIE* **10699**, 106991I (2018).
3. S. Agostinelli et al., "GEANT4: a simulation toolkit," *Nucl. Instrum. Methods* **A506**, 250–303 (2003).
4. G. Santin et al., "GRAS: a general-purpose 3-d modular simulation tool for space environment effects analysis," *IEEE Trans. Nucl. Sci.* **52**(6), 2294–2299 (2005).
5. K. Nandra et al., "The hot and energetic universe: a white paper presenting the science theme motivating the Athena+ mission," ArXiv e-prints 1306.2307, https://ui.adsabs.harvard.edu/abs/2013arXiv1306.2307N/abstract (2013).
6. A. Rau et al., "Athena wide field imager key science drivers," *Proc. SPIE* **9905**, 99052B (2016).
7. J. Aird et al., "The hot and energetic universe: the formation and growth of the earliest supermassive black holes," ArXiv e-prints 1306.2325, https://ui.adsabs.harvard.edu/abs/2013arXiv1306.2325A/abstract (2013).
8. E. Pointecouteau et al., "The hot and energetic universe: the evolution of galaxy groups and clusters," ArXiv e-prints 1306.2319, https://ui.adsabs.harvard.edu/abs/2013arXiv1306.2319P/abstract (2013).
9. S. Ettori et al., "The hot and energetic universe: The astrophysics of galaxy groups and clusters," ArXiv e-prints 1306.2322, https://ui.adsabs.harvard.edu/abs/2013arXiv1306.2322E/abstract (2013).
10. D. Lumb, J.-W. den Herder, and M. Guinazzi, "Athena science requirements document v2.6," (2020).
11. S. Lotti et al., "Review of the particle background of the Athena X-IFU instrument," *Astrophys. J.* **909**, 111 (2021).
12. E. Perinati et al., "The radiation environment in L-2 orbit: implications on the non-X-ray background of the eROSITA pn-CCD cameras," *Exp. Astron.* **33**, 39–53 (2012).
13. A. J. Tylka et al., "A revision of the cosmic ray effects on micro-electrons code," *IEE. Trans. Nucl. Sci.* 2150–2160 (1997).
14. D. Gruber, J. Matteson, and L. Peterson, "The spectrum of diffuse cosmic hard x-rays measured with HEAO-1," *Astrophys. J.* **520**, 124–129 (1999).
15. N. Marcelli et al., "Time dependence of the flux of helium nuclei in cosmic rays measured by the PAMELA experiment between 2006 July and 2009 December," *Astrophys. J.* **893**, 145 (2020).
16. O. Adriani et al., "Time dependence of the electron and positron components of the cosmic radiation measured by the PAMELA experiment between July 2006 and December 2015," *Phys. Rev. Lett.* **116**, 241105 (2016).
17. P. Dondero and A. Mantero, "A "Space dedicated" GEANT4 physics list from the AREMBES project," in *presented at the 14th Geant4 Space Users Workshop*, https://indico.esa.int/event/160/contributions/1136/ (2017).
18. V. Ivanchenko et al., "Validation of Geant4 10.3 simulation of proton interaction for space radiation effects," *Exp. Astron.* **44**, 437–450 (2017).
19. P. Dondero et al., "Electron backscattering simulation in Geant4," *Nucl. Instrum. Methods* **B425**, 18–25 (2018).
20. P. Pourrouquet et al., "FASTRAD 3.2: radiation shielding tool with a new Monte Carlo module," in *IEEE Nucl. Space Radiat. Effects Conf. – NSREC*, Las Vegas, Nevada (2011).
21. L. Pandola, C. Andenna, and B. Caccia, "Validation of the Geant4 simulation of bremsstrahlung from thick targets below 3 MeV," *Nucl. Instrum. Methods Phys. Res., Sect. B: Beam Interact. Mater. At.* **350**, 41–48 (2015).
22. M. Batič et al., "Validation of Geant4 simulation of electron energy deposition," *IEEE Trans. Nucl. Sci.* **60**, 2934–2957 (2013).
23. T. Basaglia et al., "Investigation of Geant4 simulation of electron backscattering," *IEEE Trans. Nucl. Sci.* **62**, 1805–1812 (2015).

24. A. Mantero et al., "PIXE simulation in Geant4," *X-Ray Spectrom.* **40**(3), 135–140 (2011).
25. D. J. Hall et al., "Predicting the particle-induced background for future x-ray astronomy missions: the importance of experimental validation for GEANT4 simulations," *Proc. SPIE* **10709**, 1070937 (2018).
26. e2v Technologies, "CCD97-00 back illuminated 2-phase IMO series electron multiplying CCD sensor datasheet," A1A-CCD97BI_2P_IMO, Issue 3 (2004).
27. J. H. Tutt et al., "The noise performance of electron-multiplying charge-coupled devices at soft X-Ray energy values," *IEEE Trans. Electron Devices* **59**, 2192–2198 (2012).
28. D. J. Hall and A. Holland, "Space radiation environment effects on x-ray CCD background," *Nucl. Instrum. Methods Phys. Res. Sect. A: Acceler. Spectrom. Detectors Assoc. Equip.* **612**, 320–327 (2010).
29. I. Moody et al., "CCD QE in the soft x-ray range," tech. rep., e2v Technologies (2017).
30. Advacam, "AdvaPIX TPX3 datasheet," Model No. APXMD3-Xxx170704 and APXT3M-Xxx180119 (2019).
31. M. Freyberg et al., "SRG/eROSITA in-flight background at L2," *Proc. SPIE* **11444**, 114441O (2020).
32. B. Henke, E. Gullikson, and J. Davis, "X-ray interactions: photoabsorption, scattering, transmission, and reflection at E=50-30000 eV, Z=1-92," *At. Data Nucl. Data Tables* **54**(2), 181–342 (1993).
33. C. E. Grant et al., "Reducing the Athena WFI charged particle background: results from Geant4 simulations," *Proc. SPIE* **11444**, 1144442 (2020).

**Tanja Eraerds** (nee Rommerskirchen) received her PhD in physics from Zurich University in October 2010. Since 2011, she has been working as a research assistant at the Max Planck Institute of extraterrestrial physics, where she contributed to the development of the eROSITA x-ray satellite instrument and to the Athena Wide Field Imager (WFI). Her interests include data analysis, the usage of Monte Carlo simulations for design optimizations, and the application of DEPFET detectors for space telescopes.

**David Hall** is a senior lecturer in physical sciences at the Open University. Over the last 15 years, he has worked on the simulation of instrument background, studying the background on XMM-Newton, Swift, and Suzaku. He is currently involved in the background predictions for the SMILE and THESEUS SXI instruments alongside the Athena WFI, particularly the study of graded-Z radiation shielding and the validation of Geant4 for instrument background simulations.

**Michael Hubbard** is a space radiation environment scientist at the CEI in the Open University, UK. He develops simulation frameworks and data analysis pipelines for assessing radiation background and dose rate for future space missions. Before joining the CEI, he completed his PhD at the University of Surrey, United Kingdom. Where he researched pulse shape discrimination scintillators for neutron detection. He is interested in radiation detector technology and detector modeling.

**Norbert Meidinger** is a senior staff instrument scientist and project manager at Max-Planck-Institute for extraterrestrial physics (MPE), Garching, Germany. His research areas include the development of spectroscopic x-ray detectors and instrumentation for satellites. He was engaged in the development of PNCCD detector and EPIC-PN camera for ESA's space telescope XMM-Newton. He was responsible for the eROSITA camera development with advanced PNCCD detectors and is senior CoI of eROSITA space telescope. Since the launch in 2019, he has been a member of the eROSITA operations team. Since 2013, he has been the project manager of the ATHENA Wide Field Imager (WFI).

**Emanuele Perinati** is a research collaborator at the Institute for Astronomy and Astrophysics, University of Tübingen. He conducts theoretical and experimental investigation for the development of high energy space missions. His principal area of expertise is background studies and simulations for x/gamma ray detectors.

Biographies of the other authors are not available.